



# Precision dynamic equivalent circuit model of a Vanadium Redox Flow Battery and determination of circuit parameters for its optimal performance in renewable energy applications

Ankur Bhattacharjee<sup>\*,1</sup>, Anirban Roy<sup>1</sup>, Nipak Banerjee, Snehangshu Patra, Hiranmay Saha

Centre of Excellence for Green Energy and Sensor Systems, Indian Institute of Engineering Science and Technology (IIEST), Shibpur, India



## HIGHLIGHTS

- Dynamic internal circuit parameters are estimated for VRFB system.
- The model parameters are extracted using the experimental data as input to the model.
- The dynamic internal parameter estimation model shows better performance accuracy.
- The impacts of scalability and cycle number on VRFB internal parameters are shown.
- Flow rate is optimized considering both stack internal loss and pump power loss.

## ARTICLE INFO

### Keywords:

Vanadium Redox Flow Battery (VRFB)  
Electrical equivalent circuit model  
Dynamic internal parameter extraction  
Aging factor  
Flow rate optimization  
Renewable energy integration

## ABSTRACT

In this work it is established for the first time that the internal parameters of the electrical equivalent circuit of vanadium redox flow battery (VRFB) are variable not only with flow rate and stack current but also the state of charge (SOC) and operational cycle number. The dynamic internal circuit parameters are extracted by using the charge-discharge characteristics of a practical 1 kW 6 h VRFB system as input to the proposed model. The role of temperature on the VRFB internal parameters is also discussed. It is further demonstrated that the average error in estimation of VRFB stack voltage using dynamic parameters reduces by 28% (charging) and 14% (discharging) compared to that of using static internal parameters. The proposed model exhibits robustness and validity for large scale applications as evidenced by further extracting the internal parameters of a 125 kW 2 h VRFB system. Another significant contribution of this paper is the optimization of flow rate by considering both the stack internal power loss and pump power loss simultaneously to achieve optimal performance of the VRFB system. The proposed model involving dynamic parameter extraction and loss optimization is very useful for designing suitable battery management system (BMS) for interfacing VRFB with renewable energy sources.

## 1. Introduction

The present era of fossil fuel depletion and rapid implementation of renewable energy harvesters necessitates a paradigm shift in energy storage technologies. For large-scale renewable power system applications, Vanadium Redox Flow Battery (VRFB) possesses huge potential because of its several merits; such as, independent scalability of its power and energy capacity, deep discharge capacity, free from cross-contamination and above all its very long life cycle, closely matching that of a solar PV Power Plant. The VRFB technology was invented by Maria Skyllas-Kazacos [1,2] and her research group at University of New South Wales (UNSW) in the mid-1980s. Over the years, efforts to

make the VRFB technology more efficient has led to several avenues of research –namely stack design [3–12], modifications to the electrode [13–25], membrane [26–32] and electrolyte [33–42]. The realization of practical VRFB operation and performance is incomplete without an electrical equivalent model. However, very few published papers have addressed the electrical equivalent model and internal circuit parameters estimation. A basic equivalent circuit model of a VRFB was first proposed by Barote et al. [43,44] and then followed by Chahwan et al. [45] where they introduced a voltage source, a controlled current source, a fixed resistor representing parasitic losses, two fixed internal resistors and a fixed capacitor as circuit elements. Nonetheless, their models were not realistic because they did not consider the dynamic

<sup>\*</sup> Corresponding author. ().

E-mail address: [ankur.bhattacharjee@iemcal.com](mailto:ankur.bhattacharjee@iemcal.com) (A. Bhattacharjee).

<sup>1</sup> Both the authors contributed equally to this work.

**Nomenclature**

|                                 |  |                                |   |
|---------------------------------|--|--------------------------------|---|
| $E^{0+}$                        | VRFB Positive half-cell equilibrium potential (V)  | $C_R^-$                        | Concentration of reduced vanadium species in the negative electrolyte side (mol L <sup>-1</sup> ) |
| $\alpha_a$                      | Charge transfer coefficient in the anolyte side  | $E^+$                          | Positive electrode potential (V)  |
| $\alpha_c$                      | Charge transfer coefficient in the catholyte side  | $E^-$                          | Negative electrode potential (V)  |
| $I_0$                           | Exchange current (A)   | $E_{\text{self-discharge}}$    | Self-discharge potential drop (V)   |
| $E^0$                           | VRFB Negative half-cell equilibrium potential (V)  | $R_{\text{self-discharge}}$    | Self-discharge resistance ( $\Omega$ )  |
| $E^0$                           | VRFB cell equilibrium potential (V)  | $E_{\text{Stack(OCV)}}^*$      | $E_{\text{Stack(OCV)}}$ considering self discharge potential drop (V)                             |
| SOC                             | State of Charge  | $E_t^*$                        | Stack terminal voltage considering self-discharge potential drop (V)                              |
| $I_{\text{stack}}$              | Stack current (A)  | $\tau$                         | Time constant   |
| $Q$                             | Electrolyte flow rate (L min <sup>-1</sup> )   | $R_{Ct}^c$                     | Cathodic charge transfer resistance ( $\Omega$ )  |
| $N$                             | Electrolyte capacity (A. sec cm <sup>-3</sup> )  | $R_{Ct}^a$                     | Anodic charge transfer resistance ( $\Omega$ )  |
| $n_e$                           | No. of electrons transferred per mole  | $C_{dl}^c$                     | Cathodic double layer capacitance (F)   |
| $F$                             | Faraday's constant (96485C mol <sup>-1</sup> )   | $C_{dl}^a$                     | Anodic double layer capacitance (F)   |
| $c_v$                           | Vanadium concentration (mol L <sup>-1</sup> )  | $R_0$                          | Series resistance ( $\Omega$ )  |
| $P_{\text{pump,electrical}}$    | Pump electrical power consumption (W)  | $\tilde{R}_{\text{half cell}}$ | Hydraulic resistance (Pa s m <sup>-3</sup> )  |
| $P_{\text{pump,hydraulic}}$     | Pump hydraulic power consumption (W)   | $K$                            | Dynamic viscosity of the electrolyte (Pa s)   |
| $\eta_{\text{pump}}$            | Pump efficiency  | $\mu$                          | Permeability of porous electrode  |
| $R$                             | Universal gas constant (8.3144 J K <sup>-1</sup> mol <sup>-1</sup> )                               | $\Delta p_{\text{stack}}$      | Pressure drop across the stack (Pa)   |
| $T$                             | Ambient temperature (K)  | $\Delta p_{\text{pipe}}$       | Pressure drop due to pipes (Pa)   |
| $K$                             | Proportionality constant   | $P$                            | density of the electrolyte (kg m <sup>-3</sup> )  |
| $E_{\text{Stack(OCV)}}$         | VRFB stack open circuit voltage (V)  | $V_s$                          | Velocity of the electrolyte inside the pipe (m s <sup>-1</sup> )                                  |
| $n_s$                           | No. of stacks connected in series for the entire VRFB system                                       | $Z$                            | height of the pipe (m)  |
| $n$                             | No. of series cells in VRFB stack  | $G$                            | acceleration due to gravity (m s <sup>-2</sup> )  |
| $E_{\text{Cell,eq at 50% SOC}}$ | VRFB cell equilibrium potential (V)  | $h_m$                          | minor losses (m)  |
| $I_d$                           | Diffusion current (A)  | $h_f$                          | friction losses (m)   |
| $C_i$                           | Concentration of Vanadium Species (mol L <sup>-1</sup> )   | $P_{\text{hydraulic}}$         | Pump hydraulic power consumption (Watt)   |
| $D_m$                           | Diffusion coefficient (m <sup>2</sup> s <sup>-1</sup> )  | $P_{\text{pump,electrical}}$   | Pump electrical power consumption (Watt)  |
| $x$                             | Thickness of the membrane ( $\mu\text{m}$ )  | $f$                            | friction factor   |
| $C_O^+$                         | Concentration of oxidized vanadium species in the positive electrolyte side (mol L <sup>-1</sup> ) | $L$                            | Length of pipe (m)  |
| $C_O^-$                         | Concentration of oxidized vanadium species in the negative electrolyte side (mol L <sup>-1</sup> ) | $D$                            | Hydraulic diameter of the pipe (m)  |
| $C_R^+$                         | Concentration of reduced vanadium species in the positive electrolyte side (mol L <sup>-1</sup> )  | $Re$                           | Reynolds' number  |
|                                 |  | $\eta_{\text{pump}}$           | Pump efficiency   |
|                                 |  | $\Psi$                         | Aging factor  |

nature of the parameters of a flow battery and also lacked experimental validation. In addition, an electrical equivalent model of VRFB where the RC network parameters were estimated by extended Kalman filter approach was proposed by Mohamed et al. [46,47]. However, their model did not consider the impact of practical parameters like flow rate and pump power consumption on VRFB model performance. Another unique method of identifying battery internal parameters is to perform electrochemical impedance spectroscopy (EIS) [48–50], where the RC network parameters were estimated under a wide range of frequencies. However, this technique seems to be much more complex for system level and hence applicable for single cell studies only. Therefore, modelling and simulation based studies are more prevalent. Recently, Zhang, et al. [51] introduced a comprehensive electrical equivalent circuit model of VRFB consisting of an open-circuit voltage (OCV) source, two parasitic shunt circuits, a 1st order RC network and a hydraulic circuit model signifying the pump operation. The model circuit parameters in their work were estimated by curve fitting with the experimental results of Kim et al. [52]. Yet, the dynamic nature of VRFB internal parameters was not demonstrated as a function of the state of charge (SOC) in their work. Furthermore, the optimization of electrolyte flow rate considering both aspects of minimising the internal losses and pump power consumption was not investigated. Wei et al. [53] proposed an online estimation model of VRFB State of Charge (SOC) and equivalent circuit model parameters by multi time scale estimator. In their paper the robustness of the SOC estimation model was validated by experimental result on a single VRFB cell for different flow rates and ageing levels. A MATLAB based model of VRFB was introduced by

Turkar et al. [54] and was compared with kW scale VRFB system performance. But they did not consider the flow rate optimization which plays a key role in improving the VRFB system efficiency. Tang et al. [9] proposed a flow rate optimization technique where the optimal flow rate helps in reducing pump power consumption resulting in improved VRFB system efficiency. However, in their paper, the variability of battery internal circuit parameters and associated losses were not taken into account under varying flow rates. A similar study by Averbukh et al. [55] considered only the pump loss in their flow rate optimization criteria to improve VRFB system efficiency. To realize the overall performance of a VRFB system, an electrochemical model was proposed by Blanc et al. [56] where the electrical equivalent network parameters were assumed constant for simplicity. However, for all practical applications, those parameters are observed to be variable with respect to flow rate and SOC. The performance analysis of VRFB in micro grid and power system applications was discussed by Qiu et al. [57] and Nguyen et al. [58]. These practical applications of VRFB need proper modelling and dynamically estimated parameters in order to design efficient battery management systems (BMS). A recent work published by Bhattacharjee and Saha [59] proposed a generalised electrical equivalent model of VRFB system where the dynamic optimal flow rate was estimated to improve the VRFB overall system efficiency. The model performance was demonstrated by a hybrid micro-grid system. However in their work, the internal circuit parameters were assumed to be independent of state of charge (SOC). Also the flow rate optimization criteria did not consider the dynamicity of stack internal power loss with varying flow rate.

In this paper a dynamic parameter extraction methodology is proposed. The internal parameters of VRFB electrical equivalent circuit are dynamically estimated as function of flow rate, state of charge (SOC) and stack current. The effect of operational cycle number on the VRFB internal resistance has been further estimated using a dynamic aging factor calculated from experimental results. The role of temperature on the VRFB internal parameters has also been considered. In addition to this, another significant contribution of this paper is the identification of an optimal flow rate for minimum loss in the VRFB system, considering both the pump power consumption and losses due to VRFB stack internal circuit parameters. Such a holistic approach of studying practical characteristics of a VRFB system has not been addressed in any of the existing literature. The generalised VRFB circuit model proposed is simulated in MATLAB/Simulink environment and the dynamic internal circuit parameters have been identified by using actual experimental charging and discharging characteristics as input to the model. A 20 cell 1 kW 6 h VRFB setup is used to conduct the experiments and validate the model. The model has been further utilized to extract the internal parameters of a much larger VRFB of 125 kW 2 h capacity to demonstrate its wide applicability and robustness. Thus, the model described in this work could be very useful tool for designing an efficient BMS for interfacing large-scale VRFB storage system with renewable energy sources. Finally, a design approach has been indicated in this paper for constructing the optimum electrical interfaces of VRFB at the input (renewable source) end and the output (load) end for renewable energy applications.

**Table 1**

VRFB parameters for model simulation.

| Parameters  | Quantity      | Unit                |
|---|---------------|---------------------|
| No. of series cells (n) in stack  | 20            | –                   |
| Vanadium Concentration( $c_v$ )   | 1.6           | Mol.L <sup>-1</sup> |
| Volume of electrolyte in each tank  | 180           | L                   |
| No. of electron transferred/mol ( $n_e$ )                                     | 1             | –                   |
| Dimension of each electrode<br>( $L_{felt} \times W_{felt} \times D_{felt}$ ) | 25 × 25 × 0.3 | cm × cm × cm        |
| Inner diameter of the flow pipe   | 18            | cm                  |
| Inner diameter of the guide channel   | 5             | cm                  |
| Length of the guide channel   | 117           | cm                  |
| Inner diameter of the Manifold  | 7.5           | cm                  |
| Length of the Manifold  | 42            | cm                  |
| Faraday's constant  | 96485         | C.mol <sup>-1</sup> |
| Power capacity  | 1             | kW                  |
| Energy capacity   | 6             | kWh                 |
| Voltage range   | 20–32         | Volts               |
| Maximum allowable current   | 60            | Ampere              |

## 2. Experimental setup

The experiment was performed with a 20 cell 1 kW 6 h VRFB system as shown in Fig. 1(a). The system architecture used to perform the experiment is described in Fig. 1(b). Different levels of charge-discharge current and electrolyte flow rate was controlled by dsPIC micro-controller acting as the central processor unit. Table 1 enlists the parameters of the experimental setup that were later used in the model.

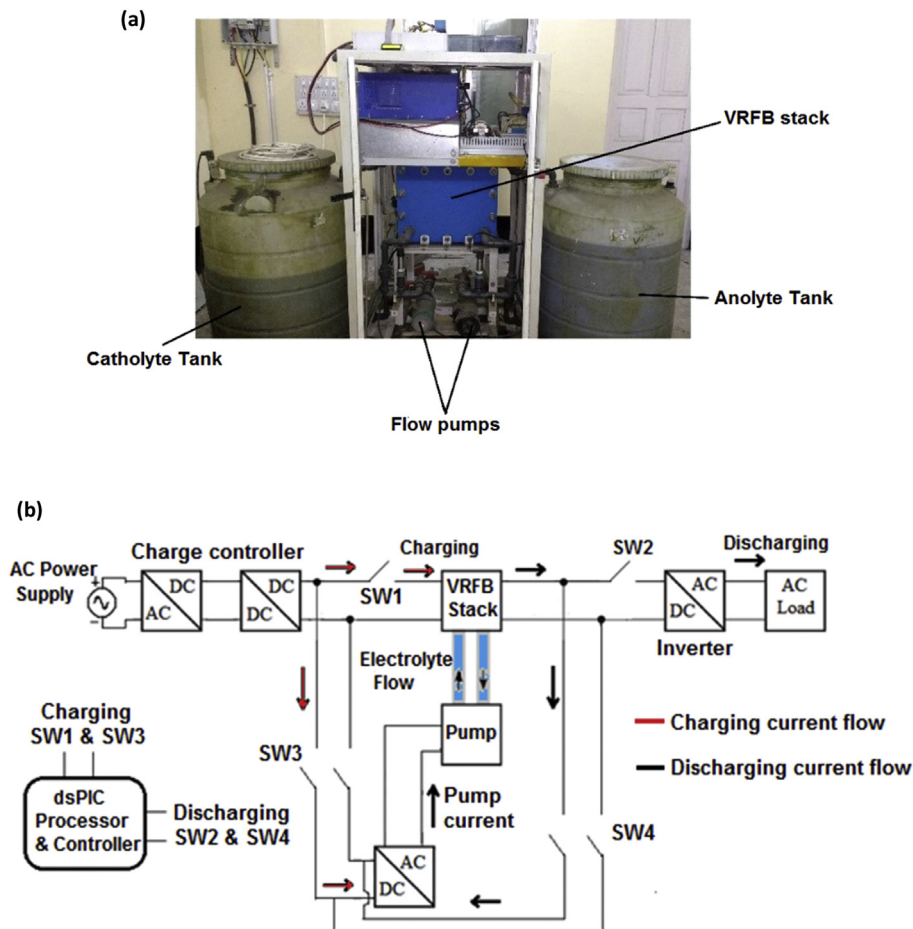


**Fig. 1.** (a). 20 Cell 1 kW 6 h VRFB experimental set up (courtesy, Big Power Electrical Technology, Xiangyang Inc. Co. Ltd China), (b). Overall block diagram representation of the experimental set up.

### 3. Experimental methodology

A commercial VRFB system of 1 kW 6 h capacity was considered for experimental study. The charging and discharging experiments were performed separately for three set of constant currents. Each set of constant current charging and discharging operation was executed under four different flow rates. Since the maximum allowable current of the VRFB was 60 A, the currents chosen for the experiment were 40 A, 45 A and 50 A respectively to ensure safe operation of VRFB. A variable

frequency drive (VFD) topology was used to control the pump for different flow rate operation. The flow rates were maintained at  $18 \text{ L min}^{-1}$ ,  $12 \text{ L min}^{-1}$ ,  $6 \text{ L min}^{-1}$  and  $3 \text{ L min}^{-1}$  respectively. It should be noted that the minimum operating flow rate maintained during the experiment was greater than the stoichiometric flow rate [60]. From the experimental study the VRFB terminal voltage characteristics were obtained and plugged into the proposed model to extract the internal parameters.

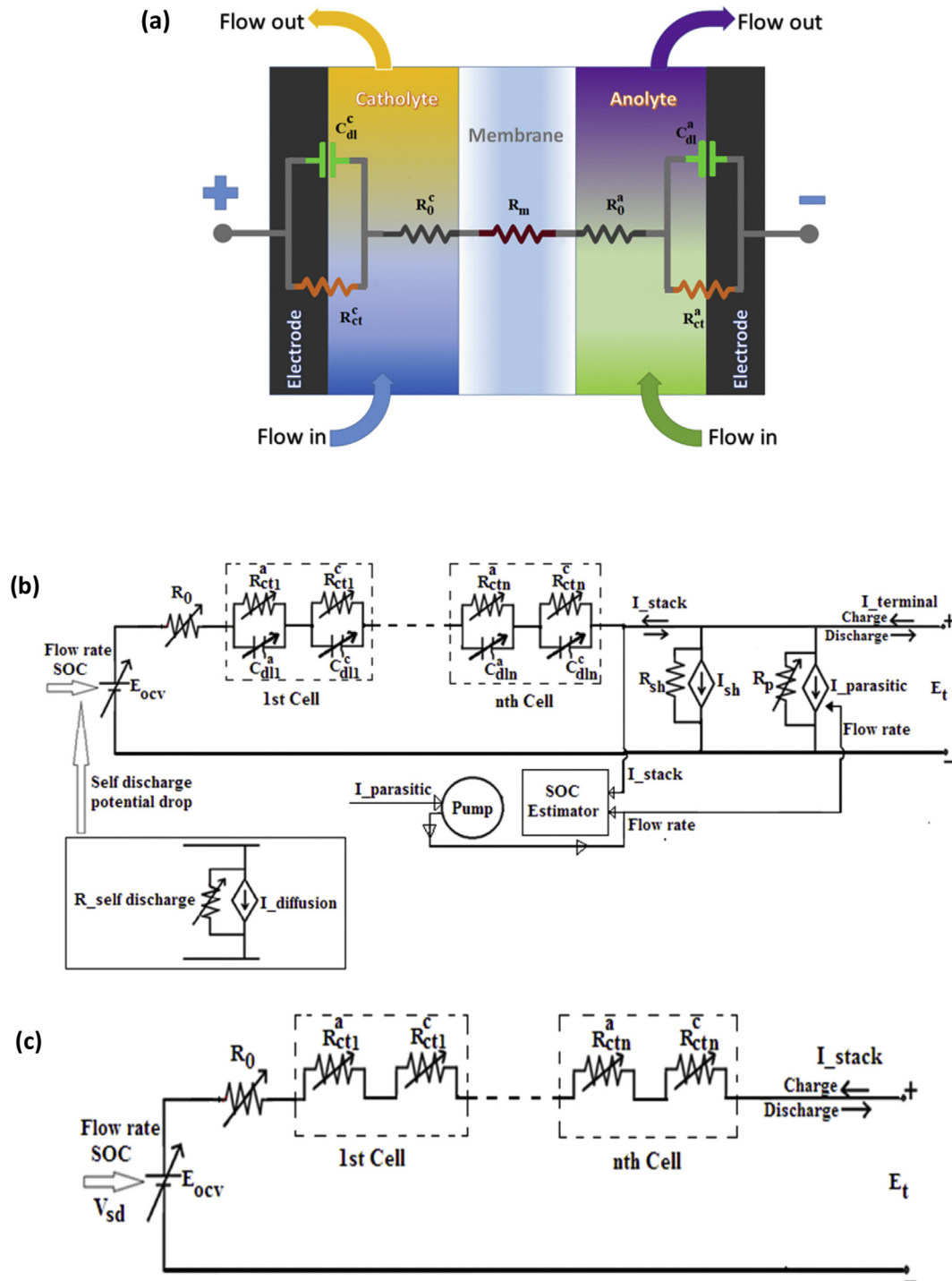


Fig. 2. (a). Realization of the internal circuit elements of a single VRFB cell, (b). Schematic of VRFB system electrical equivalent circuit, (c). VRFB electrical equivalent circuit under stationary zone of operation.

#### 4. VRFB electrical equivalent model

The internal impedance parameters of any electrochemical cell can be represented by the Randles' equivalent circuit model [61]. To understand the internal circuit parameters of a VRFB, the two half cells, proton exchange membrane and electrolyte flowing through the single cell stack are represented by corresponding internal electrical parameters in Fig. 2(a).

In Fig. 2(a), the electrochemical interface between the electrode and electrolyte is represented by a parallel combination of  $R_{ct}^c$  and  $C_{dl}^c$  in series with  $R_0^c$  which represents the positive half (Catholyte) cell electrical equivalent circuit. Similarly, the negative half (Anolyte) cell equivalent circuit is represented by the parallel combination of  $R_{ct}^a$  and  $C_{dl}^a$  in series with  $R_0^a$ .

The charge transfer resistance ( $R_{ct}$ ) is the characteristic of electrode-electrolyte interfacial configuration. It gives an idea on how the charge is transmitted across the interface during charging or discharging. The  $R_{ct}$  changes as the interface configuration is altered either by variation of the flow rate (Q) and/or with the change in concentration of vanadium ions. Thus,  $R_{ct}$  is dynamic with state of charge (SOC), flow rate (Q) and can be expressed in terms of exchange current ( $I_0$ ) by Eq. (1) [61].

$$R_{ct} = \frac{RT}{n_e F I_0} \quad (1)$$

Where, R = Universal gas constant (8.314 J). T = Ambient temperature (K).  $n_e$  = No. of electrons transferred per mol. of electrolyte solution. F = Faraday's constant (96485 C mol<sup>-1</sup>).  $I_0$  = Exchange current (A).

The exchange current is defined as the minimum threshold of current that needs to be overcome for the initiation of charge-discharge reaction.  $I_0$  is estimated using Butler-Volmer Eq. (2) [61].

$$I = I_0 \left\{ \exp \left[ \frac{\alpha_a n_e F}{RT} (E - E_{eq}) \right] - \exp \left[ -\frac{\alpha_c n_e F}{RT} (E - E_{eq}) \right] \right\} \quad (2)$$

Where, I = Terminal current (A).  $\alpha_a$  = Charge transfer coefficient in the anolyte side (Dimension less).  $\alpha_c$  = Charge transfer coefficient in the catholyte side (Dimension less). E = Electrode potential (Volts).  $E_{eq}$  = Equilibrium potential (Volts).

The  $C_{dl}$  mentioned in Fig. 2(a), is defined as the double layer capacitance which needs to be charged to initiate any electron transfer to the electrolyte. For any transient electrochemical process, the double layer current is observed to start flowing first. The double layer charging current ( $i_{dl}$ ) exponentially decays with time and becomes insignificant when the capacitor is fully charged. This signifies the end of the dynamic zone and beginning of the stationary zone in the charge-discharge profile.

In the Randles equivalent circuit in Fig. 2(a), the series element ( $R_0$ ) is introduced because the current has to pass through the electrolyte solution. This offers a solution resistance which is present in as two half-cell electrolyte resistances ( $R_0^c$  and  $R_0^a$ ) as shown in Fig. 2(a). The proton exchange membrane offers an additional resistance ( $R_m$ ). Hence the effective series resistance ( $R_0$ ) is expressed by Eq. (3);

$$R_0 = R_0^c + R_m + R_0^a \quad (3)$$

To realize a practical VRFB system consisting of multiple no. of series cells and the auxiliary subsystem like flow pump, an electrical equivalent circuit model is proposed as shown in Fig. 2(b). The terminal current is divided into three major parts starting from outside the stack to the inside; parasitic current ( $I_{parasitic}$ ) which signifies the current drawn by the two flow pumps and associated control circuit, shunt leakage current ( $I_{sh}$ ) caused by the guide and manifold channels of the VRFB stack [51]. However, this shunt current has negligibly small contribution with respect to the total terminal current as reported in established literature [51,62]. Considering this fact in this work the shunt resistance and associated shunt current is not remodelled and

taken into account to calculate the shunt loss ( $I_{sh}^2 R_{sh}$ ). The majority of the terminal current is drawn by the stack. The open circuit potential ( $E_{ocv}$ ) shown in the equivalent circuit is a function of SOC and self-discharge potential drop caused by vanadium ion diffusion under battery idle or open circuit condition and the mathematical relationship is established in the later part of section 4.1.1 of this paper.

##### 4.1. Internal parameter estimation methodology

In this work, the VRFB internal impedance parameters ( $R_0$ ,  $R_{ct}$  and  $C_{dl}$ ) are identified by fitting the experimental curve polynomial of battery terminal voltage into the parameter estimation model. From Fig. 2(b), applying loop Eq. (4),

$$Z_{int} = \frac{E_t - E_{ocv}}{\pm i_t} \quad (4)$$

Where,  $Z_{int}$  is the battery internal impedance ( $\Omega$ ).  $E_t$  is the terminal voltage across the VRFB stack terminal during charge-discharge experiment and it is the terminal current. The '+' sign implies of it implies discharging and charging conditions respectively.  $E_{ocv}$  is the open circuit voltage which is determined by the Nernst potential as function of SOC, operating temperature (T) and self-discharge potential drop.  $E_{ocv}$  is expressed by,

$$E_{ocv} = n \times \left\{ E_{eq}(at \ 50\% \ SOC) + \frac{2RT}{F} \ln \left( \frac{SOC}{1 - SOC} \right) \right\} \quad (5)$$

Where, n = No. of series connected cells.

The state of charge (SOC) mentioned in Eq. (5) is defined by

$$SOC = \frac{[V^{2+}]}{[V^{2+}] + [V^{3+}]} \quad (6)$$

Where  $[V^{2+}]$  and  $[V^{3+}]$  are the vanadium concentrations in the negative electrolyte side. Similarly the SOC can also be defined in terms of the positive electrolyte side.

##### 4.1.1. Estimation of self discharge parameters and its effect on the VRFB cell OCV

VRFB stack open circuit voltage ( $E_{ocv}$ ) is estimated by considering the effect of self-discharge which is a real life phenomenon. The self-discharge occurs due to the crossover of vanadium ions through the proton exchange membrane from both positive and negative electrolyte sides under ideal or open circuit condition. Therefore the estimation of diffusion current and equivalent self-discharge resistance is essential to realize the impact of self-discharge on the VRFB open circuit voltage ( $E_{ocv}$ ). The diffusion current is a function of the concentration gradient and diffusion coefficients of different vanadium species from two half cells at an initial SOC [63,64] and it is calculated by the following equation;

$$I_d = C_i D_m \frac{dC_i}{dx} \quad (7)$$

Where,  $I_d$  = Diffusion Current (A).  $C_i$  = Concentration of Vanadium Species (mol L<sup>-1</sup>).  $D_m$  = Diffusion coefficient (m<sup>2</sup>. s<sup>-1</sup>).  $x$  = Thickness of the membrane ( $\mu$ m).

The average concentration change (mol.L<sup>-1</sup>) of different vanadium ions from the experimental results and observations of You et al. [63]

**Table 2**

Estimated values of diffusion currents for each Vanadium ion during crossover.

| Vanadium Species | Diffusion current in the Positive half cell (Ampere) | Diffusion current in the Negative half cell (Ampere) |
|------------------|--|--|
| V <sup>2+</sup>  | –  | $1.75 \times 10^{-8}$                                |
| V <sup>3+</sup>  | $1.45 \times 10^{-8}$                                | $1.21 \times 10^{-8}$                                |
| V <sup>4+</sup>  | $3.41 \times 10^{-8}$                                | –  |
| V <sup>5+</sup>  | $2.39 \times 10^{-8}$                                | $5.12 \times 10^{-9}$                                |



and Sun et al. [64] have been used to estimate diffusion current ( $I_d$ ) for each vanadium ion while crossover through ion exchange membrane. The diffusion of vanadium ions that occurs in the positive half-cell involves the migration of  $V^{3+}$ ,  $V^{4+}$  and  $V^{5+}$ , whereas in the negative half-cell the migration of  $V^{2+}$ ,  $V^{3+}$  and  $V^{5+}$  takes place. The estimated values of  $I_d$  for each vanadium species are shown in Table 2 with a case study of an initial SOC of 90% and 40 Hours of idle observation time.

The open circuit potential for self-discharge is estimated from the Nernst potential equation considering the diffusion concentrations of vanadium species in half cells.

$$E^+(t) = E_+^{eq} + \frac{RT}{F} \ln \left( \frac{C_O^+(t)}{C_R^+(t)} \right) \quad (8)$$

$$E^-(t) = E_-^{eq} + \frac{RT}{F} \ln \left( \frac{C_O^-(t)}{C_R^-(t)} \right) \quad (9)$$

Where,  $E^+(t)$  = Positive electrode potential (Volts),  $E^-(t)$  = Negative electrode potential (Volts),  $E_+^{eq}$  = Positive electrode equilibrium potential (Volts),  $E_-^{eq}$  = Negative electrode equilibrium potential (Volts),  $C_O^+$  = Concentration of oxidized vanadium species in the positive electrolyte side ( $\text{mol.L}^{-1}$ ),  $C_O^-$  = Concentration of oxidized vanadium species in the negative electrolyte side ( $\text{mol.L}^{-1}$ ),  $C_R^+(t)$  = Concentration of reduced vanadium species in the negative electrolyte side ( $\text{mol.L}^{-1}$ ),  $C_R^-(t)$  = Concentration of reduced vanadium species in the negative electrolyte side ( $\text{mol.L}^{-1}$ ). The potential drop during self-discharge becomes,

$$E_{\text{selfdischarge}}(t) = E^+(t) - E^-(t) \quad (10)$$

The self-discharge phenomenon is presented in the VRFB electrical equivalent model by a controlled current source ( $I_{\text{diffusion,eq}}$ ) and a shunt resistance ( $R_{\text{self,discharge}}$ ) as shown in Fig. 2(a). The shunt resistance is estimated by the diffusion current and Nernst potential during crossover of vanadium species and presented by the following equation,

$$R_{\text{self,discharge}}(t) = \frac{E_{\text{self,discharge}}(t)}{I_{\text{diffusion}}(t)} \quad (11)$$

$R_{\text{self,discharge}}$  is a variable parameter which varies with the change in concentration of different vanadium species while cross over through membrane under open circuit condition over a period of time. But it is independent of charging current as the diffusion process considered in this work is under open circuit condition.

To validate Eqs. (8)–(11), a cases study of 40 h of VRFB idle observation time is considered. The self-discharge resistance ( $R_{\text{self,discharge}}$ ) for an initial SOC of 90% is estimated as 97.15 M $\Omega$  and corresponding self-discharge potential is estimated as 95.7 mV per Cell, i.e., 1.91 V for 20 series Cell VRFB System. Similarly the  $R_{\text{self,discharge}}$  can be estimated for other initial SOC levels and observation time by forming a look up table based on Eq. (11).

After considering the self-discharge effect on the  $E_{\text{Stack(OCV)}}$  estimation, the modified  $E_{\text{Stack(OCV)}}$  becomes,

$$E_{\text{Stack(OCV)}}^* = n \times \left\{ E_{\text{Cell,eq(at 50% SOC)}} + \frac{2RT}{F} \ln \left( \frac{\text{SOC}}{1 - \text{SOC}} \right) - I_d R_{\text{self,discharge}} \right\} \quad (12)$$

Where,  $E_{\text{Stack(OCV)}}^*$  = Modified  $E_{\text{Stack(OCV)}}$  after considering self discharge potential drop for certain initial SOC and open circuit observation period.

#### 4.1.2. Extraction of VRFB internal parameters under different charging time zone

To estimate the internal circuit parameters a loop equation was applied as input signal to the proposed RC equivalent circuit of VRFB in dynamic and stationary zone as shown in the simulated parameters

shown in Fig. 2(a);

The loop equations of the dynamic RC circuit are developed as;

$$E_t(t) - E_{\text{ocv}}(t) \pm I_{\text{stack}}(t)R_0(t) \pm V_{\text{Cdl}}(t) = 0 \quad (13)$$

Where  $V_{\text{Cdl}}(t) = V_{\text{Cdl}}(\tau)\{1 - \exp(-t/\tau)\}$

In Eq. (13), the  $\pm$  sign signifies the charging and discharging conditions. The '+' sign implies discharging and '-' sign implies charging of VRFB system.

$\tau$  signifies the time constant of the RC parallel circuit.

$$\tau = R_{\text{ct}}C_{\text{dl}} \\ V_{\text{Cdl}}(t') = I_{\text{stack}}(t')R_{\text{ct}}(t') \quad (14)$$

$t'$  is the time taken to reach the stationary zone in charge/discharge curves, as discussed in section 5 of this paper. In engineering practice, for the first order circuit dynamics  $t'$  is considered to be five times of  $\tau$ .

In the stationary zone the double layer capacitor of each anolyte and catholyte side become fully charged and act as open circuit elements; therefore the effective circuit parameters consist of resistors only. The modified circuit to realize the stationary zone is shown in Fig. 2(c).

The relevant loop equations in the stationary zone becomes,

$$E_t(t) - E_{\text{ocv}}(t) - I_{\text{stack}}(t)R_0(t) - n*I_{\text{stack}}(t)[R_{\text{ct}}^a + R_{\text{ct}}^c] = 0 \quad (15)$$

$$E_t(t) - E_{\text{ocv}}(t) - n*I_{\text{stack}}(t)R_{\text{int}}(t) = 0 \quad (16)$$

Where,  $R_{\text{int}} = R_0 + n*R_{\text{ct}}$  And,  $R_{\text{ct}} = R_{\text{ct}}^a + R_{\text{ct}}^c$

The above Eq. (15) and (16) is solved based on the known parameters ( $E_t$ ,  $E_{\text{ocv}}$ ,  $I_{\text{stack}}$ ) under specific terminal current and flow rates.

Considering the large scale applications of VRFB, it is a fact that the multiple stacks grouped together may exhibit inconsistencies in the distribution of stack internal resistances ( $R_{\text{int}}$ ) for the whole VRFB system. These may be caused by some physical factors like material quality of electrode, dimensions of flow channels, and mismatch in power capacity of stacks.

Therefore, the total VRFB internal resistance ( $R_{\text{int}}^*$ ) for ' $n_s$ ' no. of stacks is calculated by Eq. (17),

$$R_{\text{int}}^* = \sum_{k=1}^{n_s} R_{\text{int},k} \quad (17)$$

The VRFB internal circuit parameter extraction methodology presented in this paper is a generalised one and its performance is validated by a 1 kW 6 h VRFB system. However, for large-scale group VRFB systems, the internal circuit parameters will be scaled according to the battery specific charging and discharging characteristics that will be used as input for the extraction model.

#### 4.2. VRFB pump model formulation

The VRFB system employs two pumps whose mechanical power drives the electrolyte through the hydraulic circuit. In order to realize the pump power consumption, a formulation of the hydraulic model is essential. An analytical approach to model the hydraulic circuit and its pressure drops was shown by Blanc and Rufer [56]. In this work, the power consumed by the pump was modelled considering the associated pressure drops inside the VRFB hydraulic circuit.

Majority of the pressure drop arise due to the VRFB stack. It is reported that nearly 70% of this pressure loss is observed inside the felt electrodes [51,52]. The felt electrode can be considered of as a porous sponge and the hydraulic resistance ( $\tilde{R}_{\text{half cell}}$ ) offered by is estimated by the Darcy law given in Eq. (18) [51],

$$\tilde{R}_{\text{half cell}} = \frac{\mu L_{\text{felt}}}{kW_{\text{felt}} D_{\text{felt}}} \quad (18)$$

Where,  $k$  = permeability of porous electrode,  $\mu$  = dynamic viscosity of the electrolyte.

The total pressure drop of VRFB stack is equal to that of a single cell, because the electrolyte flows parallel through each cell inside the stack.

The total pressure drop in the stack is obtained as [51],

$$\Delta p_{\text{stack}} = 2 \times \frac{Q \tilde{R}_{\text{half cell}}}{0.7n} \quad (19)$$

The pressure drop from the pipes in the external circuit also contributes significantly to the total pressure loss of the system. The pressure drop inside the pipe is modelled using the extended Bernoulli's Eq. (20) [56],

$$\Delta p_{\text{pipe}} = -\rho g \left( \Delta \frac{V_s^2}{2g} + \Delta z + h_f + h_m \right) \quad (20)$$

Where,  $\rho$  = density of the electrolyte.  $V_s$  = Velocity of the electrolyte inside the pipe.  $z$  = height of the pipe.  $g$  = acceleration due to gravity.

The minor losses ( $h_m$ ) are given by Eq. (21),

$$h_m = K_l \frac{\Delta V_s^2}{2g} \quad (21)$$

Where,  $K_l$  = Loss co-efficient.

The different values of  $K_l$  used to model are provided in Table 3.

The friction losses ( $h_f$ ) due to flow inside the pipe is given by the Darcy-Weisbach equation,

$$h_f = f \frac{L}{D} \frac{\Delta V_s^2}{2g} \quad (22)$$

Where,  $f$  = friction factor.  $L$  = Length of pipe.  $D$  = Hydraulic diameter of the pipe.

The friction factor ( $f$ ) is dependent on the type of flow. In order to determine the nature of flow through the pipe, i.e. laminar or turbulent, the Reynolds number ( $Re$ ) is calculated as,

$$Re = \frac{\rho V_s D}{\mu} \quad (23)$$

Depending on the Reynolds' number, the friction factor ( $f$ ) is computed as,

$$f = \frac{64}{Re}, \quad Re < 2000 \quad (24)$$

And

$$f = 0.316 Re^{-0.25}, \quad 4000 < Re < 10000 \quad (25)$$

Once the total pressure drop is calculated, the hydraulic power required by the pumps is given by the equation,

$$P_{\text{hydraulic}} = Q(\Delta p_{\text{stack}} + \Delta p_{\text{pipe}}) \quad (26)$$

The pump electrical power consumption is calculated based on the pump efficiency characteristics curve shown by Li et al. [62] and it is represented by Eq. (27).

$$P_{\text{pump electrical}} = \frac{P_{\text{hydraulic}}}{\eta_{\text{pump}}} \quad (27)$$

Where,  $P_{\text{pump electrical}}$  = Pump electrical power consumption (Watt).  $P_{\text{hydraulic}}$  = Pump hydraulic power consumption (Watt).  $\eta_{\text{pump}}$  = Pump efficiency.

#### 4.3. Effect of temperature on the VRFB internal parameters

The temperature rise inside VRFB stack occurs mainly due to the heat generated from stack resistance during charging/discharging ( $I_{\text{stack}}^2 \cdot R_{\text{int}} \cdot t$ ). Therefore, along with SOC and flow rate, VRFB stack internal resistance ( $R_{\text{int}}$ ) is also a function of temperature.

From the thermodynamic equations of VRFB, the relation between stack internal resistance ( $R_{\text{int}}$ ) and stack temperature is established during charging and discharging.

$$C_p \rho V_s \frac{dT_s}{dt} = Q_+ C_p \rho (T_+ - T_s) + Q_- C_p \rho (T_- - T_s) + I_C^2 R_C \quad (28)$$

$$C_p \rho V_s \frac{dT_s}{dt} = Q_+ C_p \rho (T_+ - T_s) + Q_- C_p \rho (T_- - T_s) + I_D^2 R_D \quad (29)$$

Where,  $C_p$  = Specific heat of the electrolyte ( $\text{Jg}^{-1}\text{K}^{-1}$ ).  $\rho$  = Density of electrolyte ( $\text{gm}^{-3}$ ).  $V_s$  = Volume of VRFB stack ( $\text{m}^3$ ).  $T_s$  = VRFB stack temperature ( $^\circ\text{C}$ ).  $Q_+$  = Outlet flow rate of the positive electrolyte in the tank ( $\text{m}^3 \text{s}^{-1}$ ).  $Q_-$  = Outlet flow rate of the negative electrolyte in the tank ( $\text{m}^3 \text{s}^{-1}$ ).  $T_+$  = Temperature of the positive electrolyte in the tank ( $^\circ\text{C}$ ).  $T_-$  = Temperature of the negative electrolyte in the tank ( $^\circ\text{C}$ ).  $I_C$  = Charging current (A).  $I_D$  = Discharging current (A).  $R_C$  = VRFB stack internal resistance during charging ( $\Omega$ ).  $R_D$  = VRFB stack internal resistance during discharging ( $\Omega$ ).

Assuming uniform flow rate in both the tank outlets and the heat carried by the electrolyte from the stack to the tanks in real time, the temperature in both the tanks and the stack are almost equal for any instance of charging and discharging [65].

Therefore, the simplified form of Eq. (28) and Eq. (29) are,

$$C_p \rho V_s \frac{dT_s}{dt} = I_C^2 R_C \quad (30)$$

$$R_C = \frac{C_p \rho V_s}{I_C^2} \left( \frac{dT_s}{dt} \right) \quad (31)$$

$$R_C = R_{0\text{CHARGE}} + n * (R_{\text{ct}}^a + R_{\text{ct}}^c)_{\text{CHARGE}} \quad (32)$$

And,

$$C_p \rho V_s \frac{dT_s}{dt} = I_D^2 R_D \quad (33)$$

$$R_D = \frac{C_p \rho V_s}{I_D^2} \left( \frac{dT_s}{dt} \right) \quad (34)$$

$$R_D = R_{0\text{DISCHARGE}} + n * (R_{\text{ct}}^a + R_{\text{ct}}^c)_{\text{DISCHARGE}} \quad (35)$$

$R_C$  and  $R_D$  are determined by Eq. (31) and Eq. (34) by the battery specific known parameters ( $C_p$ ,  $\rho$ ,  $V_s$ ) and the rate of rise of VRFB stack temperature ( $T_s$ ) measured from charge-discharge experimental data. Using the methodology mentioned above, the impact of temperature on the stack internal resistance for VRFB system can be incorporated in the parameter extraction model. From the thermal behavior perspective of VRFB system, due to continuous circulation of electrolyte from the stack to the tanks it has been observed in the experiments that the temperature rise inside VRFB stack during charging and discharging lies within the range of  $29^\circ\text{C}$ – $35^\circ\text{C}$  which is well below the threshold where the thermal precipitation occurs (above  $40^\circ\text{C}$ ) [65]. Therefore the rate of change of stack temperature ( $\frac{dT_s}{dt}$ ) becomes very small over the entire range of SOC. Moreover, the difference between the inlet and outlet temperatures is very low. Hence, the correlation between VRFB storage system internal parameters and temperature comes out to be of less importance under different operating conditions set by the battery management system (BMS) in practical applications [66].

## 5. Results and discussion

The dynamic model presented in this work is validated by the charge-discharge experiments performed on a 1 kW 6 h VRFB system. The results from the experiment are given in Fig. 3. In Fig. 3(a), the VRFB stack terminal voltage data is obtained for a fixed charging

**Table 3**  
Loss coefficients for minor losses [56].

| Geometry                     | Loss coefficient $K_l$ |
|------------------------------|------------------------|
| From a reservoir into a pipe | 0.04–0.9               |
| From a pipe into a reservoir | 1                      |
| Bends and elbows             | 0.2–1.5                |
| Valves                       | 0.15–10                |

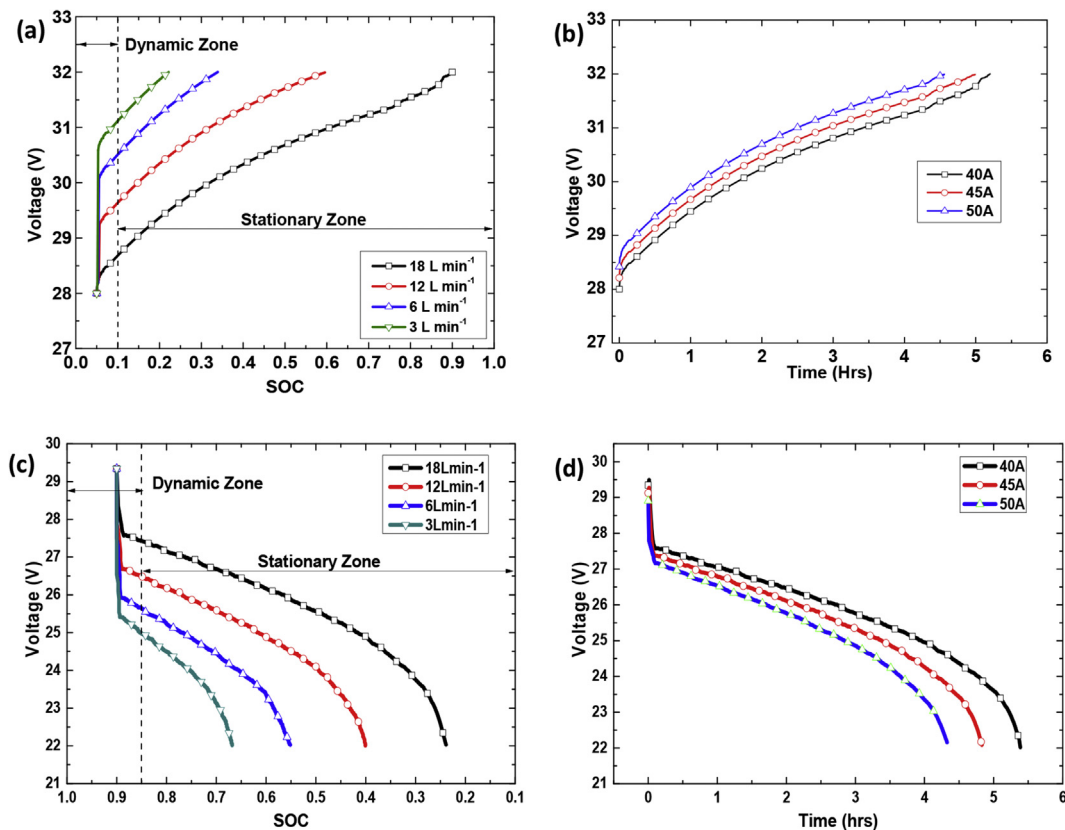


Fig. 3. (a). Experimental VRFB stack voltage at 40 A charging current and four different flow rates, (b). Experimental VRFB stack voltage at flow rate of  $18 \text{ L min}^{-1}$  and three different set of charging currents, (c). Experimental VRFB stack voltage at 40 A discharging current and four different flow rates, (d). Experimental VRFB stack voltage at flow rate of  $18 \text{ L min}^{-1}$  and three different set of discharging currents.

current and four set of flow rates. Whereas in Fig. 3(b) it is obtained for a fixed flow rate and three sets of charging currents. Similarly the data from the discharging experiments are illustrated in Fig. 3(c) and (d). In this work, for safe operation the overcharging potential of the VRFB is restricted at 32 V (for 20 cells in series, i.e. 1.6 V/cell) for all the charging experiments and the discharging potential is limited to 22 V (for 20 cells in series, i.e. 1.1 V/cell). For constant current charging and discharging, different flow rates affect the end SOC. Therefore the VRFB stack terminal voltage is represented with respect to SOC and not with time in Fig. 3(a) and (c). A fitting curve polynomial is generated from the experimental data for each charging and discharging experiment at different flow rates and currents as shown in Eq. (36);

$$f(x) = Ax^4 + Bx^3 + Cx^2 + Dx + E \quad (36)$$

Where,  $x$  is time and the polynomial coefficients  $A$ ,  $B$ ,  $C$ ,  $D$  and  $E$  are obtained by regression analysis for each experimental data set. The obtained polynomial is used as input to the proposed simulation model to extract the internal parameters by applying loop Eq. (13)–(16) in both dynamic and stationary zone of charging.

### 5.1. Extraction of dynamic internal circuit parameters of VRFB stack

The real time dynamic nature of each internal circuit parameter is shown in Fig. 4(a) and (b). The experimental curves from Fig. 3(a) and (c) show linearity after reaching the end of dynamic zone. Therefore, the variable nature of the double layer capacitor ( $C_{dl}$ ) in both anolyte ( $C_{dl,a}$ ) and catholyte ( $C_{dl,c}$ ) side are obtained with the consideration that the equivalent capacitors are fully charged at the end of the dynamic zone. From Fig. 4(a) and (b) it is observed that  $C_{dl}$  exhibits a 1st order dynamic nature which saturates at the stationary zone. The value of  $R_{ct,a}$  is found to be high compared to that of  $R_{ct,c}$ . This nature is

attributed to the difference in rate of reaction between the anode and cathode. The cathodic reaction ( $V^{5+}/V^{4+}$ ) rate appears to be faster compared to anodic reaction ( $V^{3+}/V^{2+}$ ) rate [16,18] which results in higher  $R_{ct,a}$ . As described in section 4, the  $R_{ct}$  varies with SOC and flow rate but independent of stack current. It is observed from the simulation results in Fig. 4(c) that both  $R_{ct,a}$  and  $R_{ct,c}$  undergo a very little variation with SOC over a very small range ( $R_{ct,a}$  changes from 0.00835  $\Omega$  to 0.00865  $\Omega$  and  $R_{ct,c}$  changes from 0.00205  $\Omega$  to 0.00217  $\Omega$ ). For each flow rate operation, the  $R_{ct}$  is thus treated as one of the model reference parameter for determining the  $C_{dl}$  and  $R_0$  under dynamic and stationary zone of operation. As considered in the electrical equivalent circuit of VRFB, the time constant ( $\tau = R_{ct}C_{dl}$ ) for each half cell is equal. Hence in Fig. 4(a) and (b) it is observed that the  $C_{dl,a}$  is lower than  $C_{dl,c}$ , complimentary to that of  $R_{ct,a}$  and  $R_{ct,c}$ . The series resistance  $R_0$  is dynamic over the operating range of SOC. It reduces drastically in the dynamic zone and gradually in the stationary zone with increasing SOC during charging as observed from Fig. 4(a). During discharging the  $R_0$  falls till the end of dynamic zone and then gradually increases as shown in Fig. 4(b). Although major portion of the stationary zone is more or less linear, however towards the end of stationary zone a deviation from this trend is observed. This is because the series element ( $R_0$ ) captures losses involving the kinetic, ohmic and mass transport [41,67] throughout the stationary zone. While towards the end of stationary zone the mass transport loss becomes dominant and overshadows the rest.

Based on the estimation methodology discussed in section 4.1, Table 4 and Table 5 have been constructed where the average values of each internal parameters of 20 cell 1 kW VRFB electrical equivalent circuit are presented under variable flow rate, charging and discharging currents. From both the tables it is observed that the  $R_{ct}$  and  $C_{dl}$  of anolyte and catholyte vary with flow rate but independent of currents,



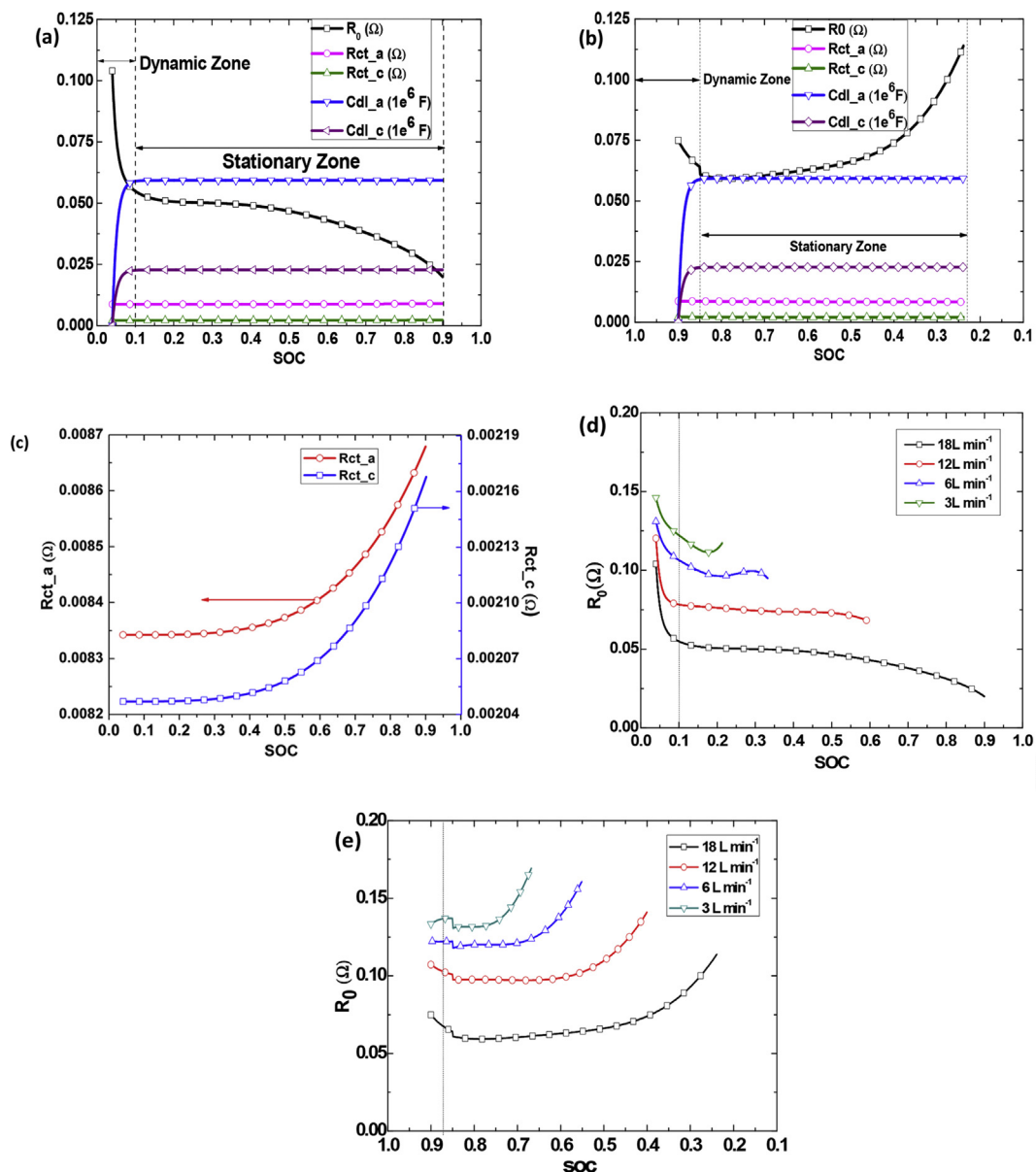


**Fig. 4.** Dynamic internal parameters of a 20 cell 1 kW VRFB over a range of SOC (5–90%) and at a flow rate of 18 L min<sup>-1</sup> and (a). charging current of 40 A. (b). discharging current of 40 A. (c). VRFB charge transfer resistance ( $R_{ct}$ ) of both catholyte and anolyte side. (d). Equivalent stack series resistance ( $R_0$ ) under varying SOC and flow rate at charging current of 40 A. (e). Equivalent stack series resistance ( $R_0$ ) under varying SOC and flow rate at discharging current of 40 A.

whereas  $R_0$  is variable with both flow rate and current. It is also observed from Tables 4 and 5 that the series resistance ( $R_0$ ) becomes significantly higher than the charge transfer resistances ( $R_{ct}$ ) for each charging and discharging current and flow rate. Therefore,  $R_0$  plays a major role in estimating the overall VRFB stack internal resistance ( $R_{int}$ ). The estimated  $R_0$  values are shown in Fig. 4(d) and (e) for 40 A charging and discharging current at four sets of flow rates. The minimum  $R_0$  is observed at the highest operating flow rate which leads to the minimum stack internal loss. This also has the added advantage of charging the battery to a higher level of end SOC.

Considering the large scale applications of VRFB storage, the parameter extraction model presented in this paper is further applied to extract the internal parameters of a 125 kW 2 h VRFB system to demonstrate the robustness and wide applicability of the model. As mentioned earlier, the charge-discharge characteristics and the stack configuration are collected from a commercial VRFB manufacturer (Big Power, China) which was then used as input for the parameter extraction model. The 125 kW VRFB comprises of 6 series stacks of 21 kW

each. The upper and lower threshold values of battery stack voltage are 650 V and 400 V respectively with rated charging current of 320 A [68]. The internal parameters extracted using the methodology discussed in section 4.1.2 is shown in Table 6.

## 5.2. Model accuracy for VRFB terminal voltage estimation

The performance of the extracted dynamic internal parameter model of VRFB and the static internal parameter for estimation of VRFB stack terminal voltage is compared with respect to the experimentally obtained VRFB stack terminal voltage shown in Fig. 5(a). As discussed in the earlier sections, the model performance is experimentally validated by 1 kW 6 h VRFB system operation. An error analysis presented in Fig. 5(b) which shows that the VRFB stack terminal voltage estimated by the proposed dynamic model gives higher accuracy for both charging and discharging experiments. The average error in VRFB stack terminal voltage considering constant internal parameters is nearly 3.5% and 7.5% during charging and discharging respectively whereas

**Table 4**

Estimation of internal circuit parameters of 1 kW 6 h VRFB under dynamic flow rates and charging currents (Average values over the complete range of SOC for each parameters are shown).

| Current | Flow rate (L. min <sup>-1</sup> ) | R <sub>0</sub> (Ω) | R <sub>ct,a</sub> (Ω) | R <sub>ct,c</sub> (Ω) | C <sub>dl,a</sub> (F) | C <sub>dl,c</sub> (F) |
|---------|-----------------------------------|--------------------|-----------------------|-----------------------|-----------------------|-----------------------|
| 40 A    | 3                                 | 0.120              | 2.89 E-02             | 5.99 E-03             | 0.24E+03              | 0.94E+03              |
|         | 6                                 | 0.102              | 0.98 E-02             | 2.04 E-03             | 0.66E+03              | 2.62E+03              |
|         | 12                                | 0.075              | 0.92 E-02             | 2.10 E-03             | 3.98E+03              | 15.7E+03              |
|         | 18                                | 0.045              | 0.85 E-02             | 2.04 E-03             | 11.6E+03              | 45.6E+03              |
| 45 A    | 3                                 | 0.126              | 2.89 E-02             | 5.99 E-03             | 0.24E+03              | 0.94E+03              |
|         | 6                                 | 0.106              | 0.98 E-02             | 2.04 E-03             | 0.66E+03              | 2.62E+03              |
|         | 12                                | 0.078              | 0.92 E-02             | 2.10 E-03             | 3.98E+03              | 15.7E+03              |
|         | 18                                | 0.048              | 0.85 E-02             | 2.04 E-03             | 11.6E+03              | 45.6E+03              |
| 50 A    | 3                                 | 0.129              | 2.89 E-02             | 5.99 E-03             | 0.24E+03              | 0.94E+03              |
|         | 6                                 | 0.109              | 0.98 E-02             | 2.04 E-03             | 0.66E+03              | 2.62E+03              |
|         | 12                                | 0.081              | 0.92 E-02             | 2.10 E-03             | 3.98E+03              | 15.7E+03              |
|         | 18                                | 0.049              | 0.85 E-02             | 2.04 E-03             | 11.6E+03              | 45.6E+03              |

**Table 5**

Estimation of internal circuit parameters of 1 kW 6 h VRFB under dynamic flow rates and discharge currents (Average values over the complete range of SOC for each parameters are shown).

| Current | Flow rate (L. min <sup>-1</sup> ) | R <sub>0</sub> (Ω) | R <sub>ct,a</sub> (Ω) | R <sub>ct,c</sub> (Ω) | C <sub>dl,a</sub> (F) | C <sub>dl,c</sub> (F) |
|---------|-----------------------------------|--------------------|-----------------------|-----------------------|-----------------------|-----------------------|
| -40 A   | 3                                 | 0.141              | 2.89 E-02             | 5.99 E-03             | 0.24E+03              | 0.94E+03              |
|         | 6                                 | 0.128              | 0.98 E-02             | 2.04 E-03             | 0.66E+03              | 2.62E+03              |
|         | 12                                | 0.105              | 0.92 E-02             | 2.10 E-03             | 3.98E+03              | 15.7E+03              |
|         | 18                                | 0.07               | 0.85 E-02             | 2.04 E-03             | 11.6E+03              | 45.6E+03              |
| -45 A   | 3                                 | 0.159              | 2.89 E-02             | 5.99 E-03             | 0.24E+03              | 0.94E+03              |
|         | 6                                 | 0.144              | 0.98 E-02             | 2.04 E-03             | 0.66E+03              | 2.62E+03              |
|         | 12                                | 0.118              | 0.92 E-02             | 2.10 E-03             | 3.98E+03              | 15.7E+03              |
|         | 18                                | 0.08               | 0.85 E-02             | 2.04 E-03             | 11.6E+03              | 45.6E+03              |
| -50 A   | 3                                 | 0.176              | 2.89 E-02             | 5.99 E-03             | 0.24E+03              | 0.94E+03              |
|         | 6                                 | 0.161              | 0.98 E-02             | 2.04 E-03             | 0.66E+03              | 2.62E+03              |
|         | 12                                | 0.131              | 0.92 E-02             | 2.10 E-03             | 3.98E+03              | 15.7E+03              |
|         | 18                                | 0.09               | 0.85 E-02             | 2.04 E-03             | 11.6E+03              | 45.6E+03              |

these errors reduce to approximately 0.2% and 1% for the model comprising of dynamic internal parameters. These results show significant accuracy of the model performance (error reduced by 28% during charging and 14% during discharging) using dynamic internal parameters compared to that of using static parameters. Such a precise model is very important so that a suitable BMS can continuously monitor and compare the battery stack terminal voltages at different SOC levels to ensure proper battery charging and discharging during practical applications.

**Table 6**

Estimation of internal circuit parameters of 125 kW 2 h VRFB under dynamic flow rates and rated charge-discharge current of 320 A (Average values over the complete range of SOC for each parameters are shown).

| Current              | Flow rate (L. min <sup>-1</sup> ) | R <sub>0</sub> (Ω) | R <sub>ct,a</sub> (Ω) | R <sub>ct,c</sub> (Ω) | C <sub>dl,a</sub> (F) | C <sub>dl,c</sub> (F) |
|----------------------|-----------------------------------|--------------------|-----------------------|-----------------------|-----------------------|-----------------------|
| 320 A (Charging)     | 20                                | 0.6                | 14.45E-02             | 29.95E-03             | 1.2E+03               | 4.7E+03               |
|                      | 40                                | 0.51               | 4.9E-02               | 10.2E-03              | 3.3E+03               | 13.1E+03              |
|                      | 80                                | 0.375              | 4.6E-02               | 10.5E-03              | 19.9E+03              | 78.5E+03              |
|                      | 100                               | 0.225              | 4.25E-02              | 10.2E-03              | 58E+03                | 228E+03               |
| -320 A (Discharging) | 20                                | 0.705              | 14.45E-02             | 29.95E-03             | 1.2E+03               | 4.7E+03               |
|                      | 40                                | 0.64               | 4.9E-02               | 10.2E-03              | 3.3E+03               | 13.1E+03              |
|                      | 80                                | 0.525              | 4.6E-02               | 10.5E-03              | 19.9E+03              | 78.5E+03              |
|                      | 100                               | 0.35               | 4.25E-02              | 10.2E-03              | 58E+03                | 228E+03               |

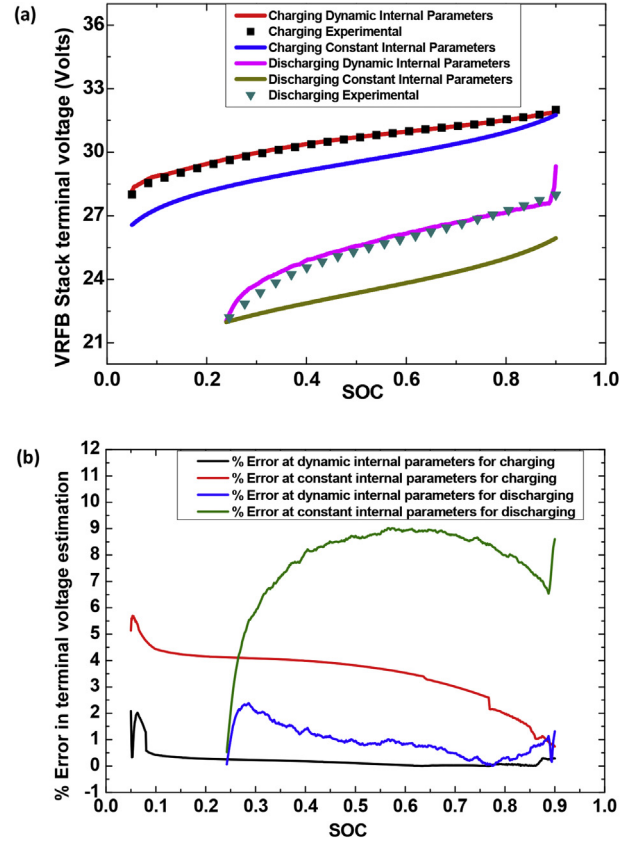


**Fig. 5.** (a). Comparison among the estimated VRFB stack terminal voltages by dynamic and constant internal parameter extraction and experimental results for 40 A charging and discharging at 18 L min<sup>-1</sup>, (b). Comparison between the errors in estimation of VRFB stack terminal voltages by dynamic and constant internal parameter extraction.

### 5.3. Effect of operational cycle number on the internal parameters of VRFB stack

Like the other batteries, the internal resistances of VRFB also undergo changes with increasing operational cycles. These changes in the internal parameters with increase in cycle number is further investigated and determined to ensure robustness and wide applicability of the proposed model. A dynamic aging factors (A.F.) for the VRFB internal resistances have been calculated by normalising the resistances obtained from the experimental work of Derr et al. [49,69] as shown in Fig. 6(a). In order to predict the aging factor ( $\psi$ ) for  $R_0$  with increasing operational cycles, a fitting polynomial of straight line with a positive slope has been chosen as shown in Eq. (37).

$$\psi = A'x + B' \quad (37)$$

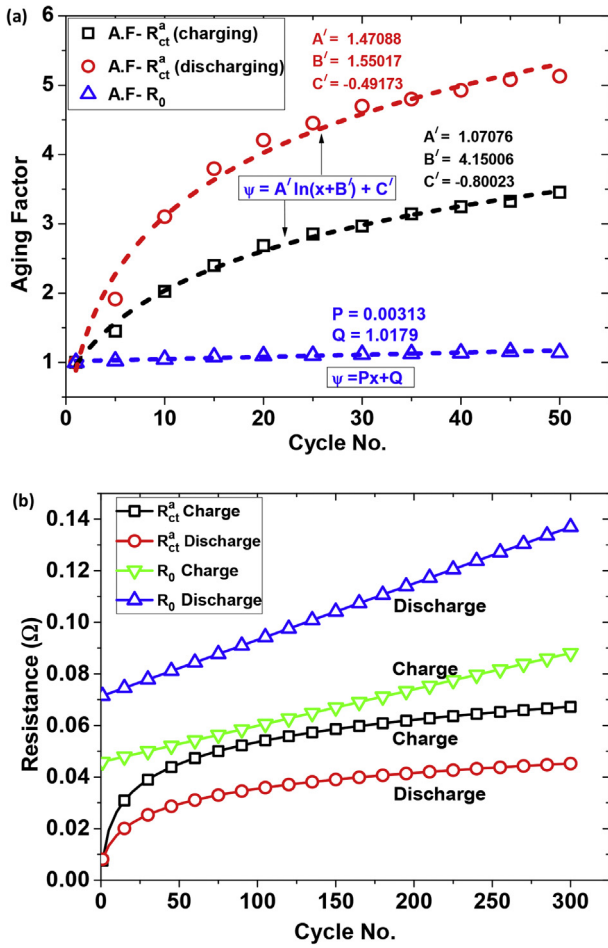


Fig. 6. Effect of increased no. of cycles on the VRFB internal resistances. (a) Dynamic aging factor (A.F) calculation by experimental curve fitting. (b) Predicted internal resistances for 300 cycles.

Similarly, the aging factor ( $\psi$ ) for calculating  $R_{ct}^a$  with increasing operational cycles is determined by fitting a logarithmic polynomial shown in Eq. (38).

$$\Psi = A' \ln(x + B') + C' \quad (38)$$

Where,  $\Psi$  = Aging factor and  $x$  = No. of cycles.  $A'$ ,  $A'$ ,  $A'B'$ ,  $C'$  are the coefficients of polynomial and determined for predicting the stack internal resistances.

Based on the polynomials obtained in Eq. (37) and Eq. (38), the dynamic aging factor for each resistance parameter is extrapolated for 300 cycles. In order to predict the internal resistances of VRFB stack for increased cycle number, the dynamic resistances obtained from the parameter extraction model for the first cycle needs to be multiplied by its corresponding aging factors. The methodology developed in this work is a generalised one and thus can be used to calculate the aging factor in case of different power capacity of VRFB for predicting its internal resistances as the cycle number increases.

Using this method, the stack internal resistances of the 1 kW 6 h VRFB is predicted for 300 cycles operating at charge-discharge current of 40 A with flow rate of  $18 \text{ L min}^{-1}$  as shown in Fig. 6(b). It is to be noted that in Fig. 6(b) the change in the charge transfer resistance of the negative half cell ( $R_{ct}^a$ ) with increasing number of cycles has been shown. The primary reason for aging in the negative half-cell is observed due to the evolution of hydrogen, which alters the surface of the felt reducing the available electrochemical surface area [49,69]. On the other hand, as described by Derr et al. [69] the positive half-cell of VRFB does not show any significant loss of performance during long

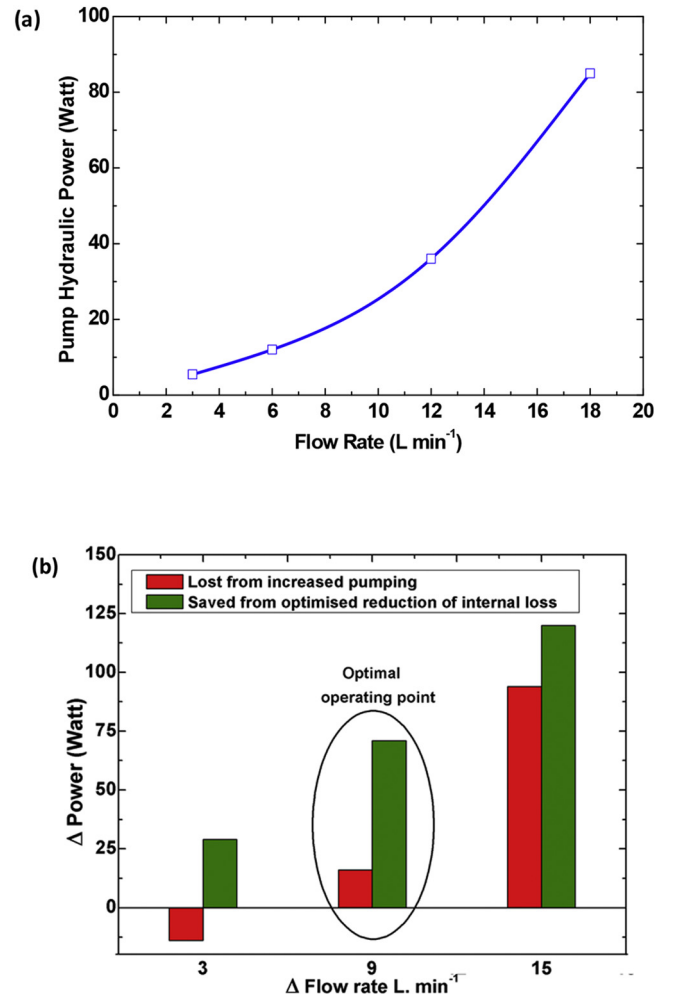


Fig. 7. (a). Pump hydraulic power consumption under different flow rates, (b). Comparison between powers lost (Due to increased pump electrical power) and saved (Due to reduction of  $R_{int}$ ) for transition of flow rates.

term cycling. Moreover, the positive half-cell charge transfer resistance ( $R_{ct}^c$ ) at any SOC is negligibly small compared to that of the negative half-cell. Therefore, the negative half-cell is considered to be the rate determining factor for VRFB. Thus we have neglected the aging of the positive half-cell resistance.

#### 5.4. Flow rate optimization

The internal electrical parameter extraction has major utility in estimating the VRFB system efficiency while designing a BMS for power system applications. As the equivalent circuit parameters are seen to vary with flow rate, an optimal rate of electrolyte flow should be identified in order to find the minimum internal power loss ( $I_{stack}^2 R_{int}$ ) inside the VRFB stack. From Tables 4 and 5 in section 5.1, it has been found that the  $R_{int}$  becomes the minimum at a flow rate of  $18 \text{ L min}^{-1}$  and 40 A charging and discharging current.

Considering the VRFB overall system efficiency, the power consumed by the flow pumps is also a significant factor besides the power loss due to stack internal resistance. The hydraulic power consumed by the pumps operating at different flow rates has been shown in Fig. 7(a). It is observed that with increasing flow rate the pump power consumption also increases exponentially. Using Eq. (26) the hydraulic power is converted to the equivalent electrical power lost during pumping. A comparative analysis has been represented in Fig. 7(b) where the change in power saved (Green coloured bar) by optimized reduction of VRFB internal resistance ( $R_{int}$ )





## Acknowledgements

All the authors whole heartedly thank Ministry of New and Renewable Energy (MNRE) Govt. of India (31/40/2010/11/ PVSE) for generous research funding to create a centre of excellence (COE) at IEST, Shibpur, India. A Bhattacharjee, A Roy and N Banerjee are thankful to IEST, India for granting research fellowships. S. Patra thanks INSPIRE Faculty award for research funding.

## References

- [1] M. Rychcik, M. Skyllas-Kazacos, *J. Power Sources* 19 (1987) 45–54.
- [2] M. Rychcik, M. Skyllas-Kazacos, *J. Power Sources* 22 (1988) 59–67.
- [3] Q. Xu, T.S. Zhao, P.K. Leung, *Appl. Energy* 105 (2013) 47–56.
- [4] J. Kim, H. Park, *Appl. Energy* 206 (2017) 451–457.
- [5] T. Wang, J. Fu, M. Zheng, Z. Yu, *Appl. Energy* (2017), <http://dx.doi.org/10.1016/j.apenergy.2017.07.065> Available online 26 July 2017, In Press.
- [6] L. Li, S. Kim, W. Wang, M. Vijayakumar, Z. Nie, B. Chen, J. Zhang, G. Xia, J. Hu, G. Graff, J. Liu, Z. Yang, *Adv. Energy Mater.* 1 (2011) 394–400.
- [7] A. Parasuraman, T.M. Lim, C. Menictas, M. Skyllas-Kazacos, *Electrochim. Acta* 101 (2013) 27–40.
- [8] M.H. Chakrabarti, N.P. Brandon, S.A. Hajimolana, F. Tariq, V. Yufit, M.A. Hashim, M.A. Hussain, C.T.J. Low, P.V. Aravind, *J. Power Sources* 253 (2014) 150–166.
- [9] A. Tang, J. Bao, M. Skyllas-Kazacos, *J. Power Sources* 248 (2014) 154–162.
- [10] M. Ulaganathan, V. Aravindan, Q.Y. Yan, S. Madhavi, M. Skyllas-Kazacos, T.M. Lim, *Adv. Mater. Interfaces* 3 (2016) 22.
- [11] L.F. Arenas, C. Ponce de León, F.C. Walsh, *J. Energy Storage* 11 (2017) 119–153.
- [12] Y. Yan, M. Skyllas-Kazacos, J. Bao, *J. Energy Storage* 11 (2017) 104–118.
- [13] E. Sum, M. Skyllas-Kazacos, *J. Power Sources* 15 (1985) 179–190.
- [14] E. Sum, M. Rychcik, M. Skyllas-Kazacos, *J. Power Sources* 16 (1985) 85–95.
- [15] B. Sun, M. Skyllas-Kazacos, *Electrochim. Acta* 36 (1991) 513–517.
- [16] G. Oriji, Y. Katayama, T. Miura, *Electrochim. Acta* 49 (2004) 3091–3095.
- [17] M. Gattrell, J. Park, B. MacDougall, J. Apte, S. McCarthy, C. Wu, *J. Electrochem. Soc.* 151 (2004) A123–A130.
- [18] G. Oriji, Y. Katayama, T. Miura, *J. Power Sources* 139 (2005) 321–324.
- [19] P. Han, Y. Yue, Z. Liu, W. Xu, L. Zhang, H. Xu, S. Dong, G. Cui, *Energy Environ. Sci.* 4 (2011) 4710–4717.
- [20] P. Han, H. Wang, Z. Liu, X. Chen, W. Ma, J. Yao, Y. Zhu, G. Cui, *Carbon* 49 (2011) 693–700.
- [21] C. Flox, J. Rubio-Garcia, R. Nafria, R. Zamani, M. Skoumal, T. Andreu, J. Arbiol, A. Cabot, J.R. Morante, *Carbon* 50 (2012) 2372–2374.
- [22] K.J. Kim, M.-S. Park, J.-H. Kim, U. Hwang, N.J. Lee, G. Jeong, Y.-J. Kim, *Chem. Commun.* 48 (2012) 5455–5457.
- [23] B. Li, M. Gu, Z. Nie, X. Wei, C. Wang, V. Sprenkle, W. Wang, *Nano Lett.* 14 (2014) 158–165.
- [24] O. Di Blasi, N. Briguglio, C. Busacca, M. Ferraro, V. Antonucci, A. Di Blasi, *Appl. Energy* 147 (2015) 74–81.
- [25] A. Di Blasi, C. Busacca, O. Di Blasia, N. Briguglio, G. Squadrito, V. Antonucci, *Appl. Energy* 190 (2017) 165–171.
- [26] H. Prifti, A. Parasuraman, S. Winardi, T.M. Lim, M. Skyllas-Kazacos, *Membranes* 2 (2012) 275.
- [27] D. Reed, E. Thomsen, W. Wang, Z. Nie, B. Li, X. Wei, B. Koeppel, V. Sprenkle, *J. Power Sources* 285 (2015) 425–430.
- [28] Y. Zhao, M. Li, Z. Yuan, X. Li, H. Zhang, I.F.J. Vankelecom, *Adv. Funct. Mater.* 26 (2016) 210–218.
- [29] X. Wei, B. Li, W. Wang, *Polym. Rev.* 55 (2015) 247–272.
- [30] X. Li, H. Zhang, Z. Mai, H. Zhang, I. Vankelecom, *Energy Environ. Sci.* 4 (2011) 1147–1160.
- [31] H. Zhang, H. Zhang, F. Zhang, X. Li, Y. Li, I. Vankelecom, *Energy Environ. Sci.* 6 (2013) 776–781.
- [32] O. David, K. Percin, T. Luo, Y. Gendel, M. Wessling, *J. Energy Storage* 1 (2015) 65–71.
- [33] F. Rahman, M. Skyllas-Kazacos, *J. Power Sources* 189 (2009) 1212–1219.
- [34] M. Vijayakumar, L. Li, G. Graff, J. Liu, H. Zhang, Z. Yang, J.Z. Hu, *J. Power Sources* 196 (2011) 3669–3672.
- [35] S. Kim, M. Vijayakumar, W. Wang, J. Zhang, B. Chen, Z. Nie, F. Chen, J. Hu, L. Li, Z. Yang, *Phys. Chem. Chem. Phys.* 13 (2011) 18186–18193.
- [36] M. Vijayakumar, W. Wang, Z. Nie, V. Sprenkle, J. Hu, *J. Power Sources* 241 (2013) 173–177.
- [37] X.L. Zhou, T.S. Zhao, L. An, Y.K. Zeng, X.H. Yan, *Appl. Energy* 158 (2015) 157–166.
- [38] Y.-S. Chou, N.-Y. Hsu, K.-T. Jeng, K.-H. Chen, S.-C. Yen, *Appl. Energy* 182 (2016) 253–259.
- [39] Y. Zhang, L. Liu, J. Xi, Z. Wu, X. Qiu, *Appl. Energy* 204 (2017) 373–381.
- [40] E. Hollman, Department of Chemical and Biomolecular Engineering, University of Tennessee, Knoxville, Tennessee, USA, 2015.
- [41] M. Skyllas-Kazacos, L. Cao, M. Kazacos, N. Kausar, A. Mousa, *ChemSusChem* 9 (2016) 1521–1543.
- [42] C. Choi, S. Kim, R. Kim, Y. Choi, S. Kim, H.-y. Jung, J.H. Yang, H.-T. Kim, *Renew. Sustain. Energy Rev.* 69 (2017) 263–274.
- [43] L. Barote, C. Marinescu, M. Georgescu, 2009 IEEE Bucharest PowerTech, 2009, pp. 1–6.
- [44] L. Barote, C. Marinescu, 2009 International Conference on Clean Electrical Power, 2009, pp. 253–257.
- [45] J. Chahwan, C. Abbey, G. Joos, 2007 IEEE Canada Electrical Power Conference, 2007, pp. 387–392.
- [46] M.R. Mohamed, H. Ahmad, M.N.A. Seman, S. Razali, M.S. Najib, *J. Power Sources* 239 (2013) 284–293.
- [47] M.R. Mohamed, H. Ahmad, M.N. Abu Seman, *Elektronika ir elektrotehnika* 19 (2013) 37–42.
- [48] J.G. Zhu, Z.C. Sun, X.Z. Wei, H.F. Dai, *J. Power Sources* 274 (2015) 990–1004.
- [49] I. Derr, M. Bruns, J. Langner, A. Fetyan, J. Melke, C. Roth, *J. Power Sources* 325 (2016) 351–359.
- [50] C.N. Sun, F.M. Delnick, D.S. Aaron, A.B. Papandrew, M.M. Mench, T.A. Zawodzinski, *J. Electrochem. Soc.* 161 (2014) A981–A988.
- [51] Y. Zhang, J. Zhao, P. Wang, M. Skyllas-Kazacos, B. Xiong, R. Badrinarayanan, *J. Power Sources* 290 (2015) 14–24.
- [52] S. Kim, E. Thomsen, G. Xia, Z. Nie, J. Bao, K. Recknagle, W. Wang, V. Viswanathan, Q. Luo, X. Wei, A. Crawford, G. Coffey, G. Maupin, V. Sprenkle, *J. Power Sources* 237 (2013) 300–309.
- [53] Z. Wei, T.M. Lim, M. Skyllas-Kazacos, N. Wai, K.J. Tseng, *Appl. Energy* 172 (2016) 169–179.
- [54] B. Turker, S. Arroyo Klein, E.-M. Hammer, B. Lenz, L. Komsijska, *Energy Convers. Manag.* 66 (2013) 26–32.
- [55] M. Averbukh, A. Pozin, S. Sukoriansky, *J. Energy Eng.* 143 (2017).
- [56] C. Blanc, A. Rufer, Understanding the vanadium Redox flow batteries, in: D.A. Ng (Ed.), *Paths to Sustainable Energy*, InTech, Europe, 2010, pp. 333–358.
- [57] X. Qiu, T.A. Nguyen, J.D. Guggenberger, M.L. Crow, A.C. Elmore, *IEEE Trans. Smart Grid* 5 (2014) 1592–1601.
- [58] T.A. Nguyen, X. Qiu, I.J.D. Guggenberger, M.L. Crow, A.C. Elmore, *IEEE Trans. Sustainable Energy* 5 (2014) 1379–1388.
- [59] A. Bhattacharjee, H. Saha, *J. Energy Storage* 13 (2017) 220–232.
- [60] M. Skyllas-Kazacos, C. Menictas, T. Lim, 12-Redox flow batteries for medium- to large-scale energy storage A2-Melhem, Ziad, *Electricity Transmission, Distribution and Storage Systems*, Woodhead Publishing, 2013, pp. 398–441.
- [61] A.J. Bard, L.R. Faulkner, *Electrochemical Methods: Fundamentals and Applications*, second ed., Wiley, 2000.
- [62] Y. Li, X. Zhang, J. Bao, M. Skyllas-Kazacos, *J. Energy Storage* 11 (2017) 191–199.
- [63] D. You, H. Zhang, C. Sun, X. Ma, *J. Power Sources* 196 (2011) 1578–1585.
- [64] J. Sun, D. Shi, H. Zhong, X. Li, H. Zhang, *J. Power Sources* 294 (2015) 562–568.
- [65] A. Tang, S. Ting, J. Bao, M. Skyllas-Kazacos, *J. Power Sources* 203 (2012) 165–176.
- [66] F. Baccino, M. Marinelli, P. Nørgård, F. Silvestro, *J. Power Sources* 254 (2014) 277–286.
- [67] A.M. Pezeshki, J.T. Clement, G.M. Veith, T.A. Zawodzinski, M.M. Mench, *J. Power Sources* 294 (2015) 333–338.
- [68] B. Power (Ed.), VBS-VI-125, Big Power, China, 2016.
- [69] I. Derr, D. Przyrembel, J. Schweer, A. Fetyan, J. Langner, J. Melke, M. Weinelt, C. Roth, *Electrochim. Acta* 246 (2017) 783–793.